A soft robot structure with limbless resonant, stick and slip locomotion

Luigi Calabrese[1,2] ⓘ**, Alice Berardo**[1]**, Danilo De Rossi**[2,3]**, Massimiliano Gei**[4] ⓘ**, Nicola Maria Pugno**[1,5,6,8] ⓘ **and Gualtiero Fantoni**[7,9]

[1] Laboratory of Bio-Inspired and Graphene Nanomechanics, Department of Civil, Environmental and Mechanical Engineering, University of Trento, via Mesiano 77, I-38123 Trento, Italy
[2] Research Centre 'E. Piaggio', University of Pisa, largo L. Lazzarino 2, I-56122 Pisa, Italy
[3] Department of Information Engineering, University of Pisa, via G. Caruso 16, I-56122 Pisa, Italy
[4] School of Engineering, Cardiff University, The Parade, Cardiff CF24 3AA, Wales, United Kingdom
[5] School of Engineering and Materials Science, Queen Mary University of London, Mile End Road, London E1 4NS, United Kingdom
[6] Ket-Lab, Edoardo Amaldi Foundation, via del Politecnico snc, I-00133 Roma, Italy
[7] Department of Civil and Industrial Engineering, University of Pisa, largo L. Lazzarino 2, I-56122 Pisa, Italy

E-mail: g.fantoni@ing.unipi.it and nicola.pugno@unitn.it

Abstract
We present a smart robot structure that exploits anisotropic friction to achieve stick-slip locomotion. The robot is made out of three components: a plastic beam, a planar dielectric elastomer actuator and four bristle pads with asymmetric rigid metallic bristles. We show that when the robot is electronically activated at increasing frequency, its structure exploits the resonance condition to reach the maximum locomotion speed. The fundamental frequency of the structure is estimated both analytically and numerically, allowing the range of frequencies in which the top locomotion speed was observed during the experiments to be identified. The locomotion speed of the robot as a function of the actuation frequency is estimated with a frequency response analysis performed on a discretised model of the structure, revealing good agreement with the experimental evidence.

Keywords: actuator, dielectric elastomer, electroactive polymer, frictional anisotropy, resonator, soft robotics

(Some figures may appear in colour only in the online journal)

1. Introduction

Nature has always been a source of inspiration for man to construct a large variety of artefacts. Hence, on the one hand, a large variety of artefacts have been made, all possessing, to some extent, life-like features. On the other, the world of modern technology is populated by machines made of strong, rigid, inorganic materials which exploit thermo-mechanical, electromagnetic and pneumatic/hydraulic energy conversion principles. In very recent years the field of robotics has seen a fast-growing interest and momentum in emerging knowledge of mechanism and materials exploited by natural organism to accomplish their living functions. Biologically inspired design [1], artificial ethology [2], artificial life [3], bio-robotics [4] and soft robotics [5] are different fields in which these tendencies manifest themselves.

The propulsion and locomotion strategies proper of different animal species have been of interest to biologists for centuries and strongly revisited these days [6]. Boneless and limbless soft-bodied animals have recently attracted the interest of engineers trying to capture strategies and replicate functions that different species use for survival in different environments. Crawling, ciliary swimming, climbing, digging and burrowing, regulation of particles-surface interactions and peristaltic transport are all functions under scrutiny by bio-inspired designers.

---

[8] Co-corresponding author.
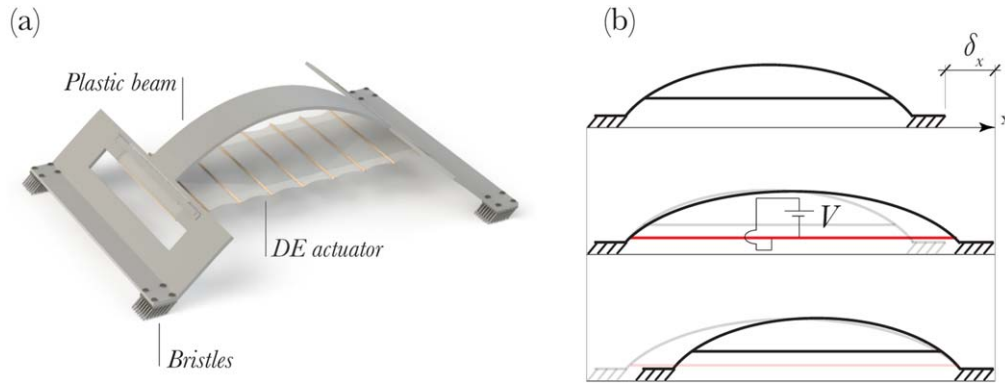[9] Corresponding author.

Figure 1. Schematic drawing of the locomotion robot (a) consisting of an assembly of three components: a plastic beam, a dielectric elastomer actuator and four clawed pads featuring rigid bristles with an asymmetric orientation. The locomotion cycle (b) starts from the initial self-standing configuration (top); when a voltage V is applied to the DEA, an elongation is induced resulting in a forward slip of the front bristles (centre); finally, when the voltage is switched off the DEA shrinks, resulting in a forward slip of the back bristles (bottom).

Inspired by the kinematics of inchworms, crawling robots consisting of a deformable body driven by Dielectric Elastomer Actuators (DEAs) have been recently reported in literature. In particular, on the one hand, crawling robots based on the principle of unimorph bending were proposed to be able to reach locomotion speeds up to approximately one body length per second without any need of pre-stretching the elastomer [7]. On the other, saddle-like robots, while requiring a deformable structure to hold a prestretched DEA around a minimum energy configuration [8], have shown the capability to achieve higher locomotion speeds, in the order of several body lengths per second [9]. This kind of robot however presents a complex manufacturing procedure. Indeed, since the saddle shape is achieved upon demolding, when the robot bends to its rest state, it is practically impossible to tune its shape after the manufacturing in case of need. To overcome this issue, a possibility is to couple the DEA with an arch-like beam, which easily allows: (i) the tuning of the length of the robot during the manufacturing phase, (ii) the compensation for the creep deformation occurring at a later stage, and (iii) the replacement of the DEA in case of rupture.

Following this approach, in this paper, we describe a smart structure endowed with locomotion capabilities which combine resonant activation [10] and anisotropic friction [11]. While operation at resonance provides a minimum in energy consumption and speed changes, still maintaining this energy minimum, by simply tuning body resonance, functional anisotropy offers valid design options for direction-dependent or orientation-dependent sliding [12]. The structure is actuated by a dielectric elastomer actuator which, in addition to fast, silent large stroke and durability [13], also has the capacity of self–sensing [14] which easily enables closed-loop control [15].

2. Materials and methods

2.1. Concept design

The robot presented in this work consists of an assembly of three components: a plastic beam, a planar DEA and four bristle pads with asymmetric rigid bristles, see figure 1(a).

Since the actuator behaves as a spring with initial pretension (as better explained in the following), when coupled to the bent plastic beam it results in a self-standing structure in which elastic energy is stored. From this configuration (figure 1(b), top), owing to the capability of the dielectric elastomer membrane to elongate upon application of a driving voltage V [16], a part of the stored elastic energy is released, allowing the robot to deform by increasing its length (figure 1(b), centre): the back bristles stick to the ground and the front bristles slip forward. In a second phase, when the voltage V is switched off, the DEA shortens, returning to its original length. This triggers the forward slip of the back bristles while the front bristles are stuck to the ground resulting in an overall net displacement δ_x (figure 1(b), bottom). What is here described as a simple sequence of two steps can be enhanced by exploiting the vibration properties of the structure and impose an on-off frequency of the voltage signal close to the resonance frequency of the robot.

2.2. Robot components

2.2.1. Dielectric elastomer actuator.
DEAs are electromechanical transducers consisting of a thin layer of a dielectric elastomer coated on both sides with compliant electrodes. When a voltage V is applied across the electrodes, the attraction electrostatic forces squeezes the soft dielectric layer causing a reduction of its thickness and an expansion of its surface [16]. Since in our case only a unidirectional actuation along the longitudinal direction was needed, we equipped the DEA with stiffening elements aligned in the transverse direction, as previously reported to be effective for this purpose [17, 18]. The DEA was manufactured by coupling two layers of an acrylic elastomer film (VHB 4910, 3 M, USA), each of them featuring a thickness at rest of 1 mm, a width of 12.5 mm and a length of 17.5 mm, chosen because of its well-known high electromechanical transduction performance in terms of achievable active stress and actuation speed. To manufacture the actuator, the two VHB 4910 membranes were equi-biaxially pre-stretched by 300% and attached to individual support frames allowing for obtaining an actuator with a length of 70 mm and a width of 50 mm. At this stage, such pre-strain caused a thickness reduction of the coupled layers from 2 to
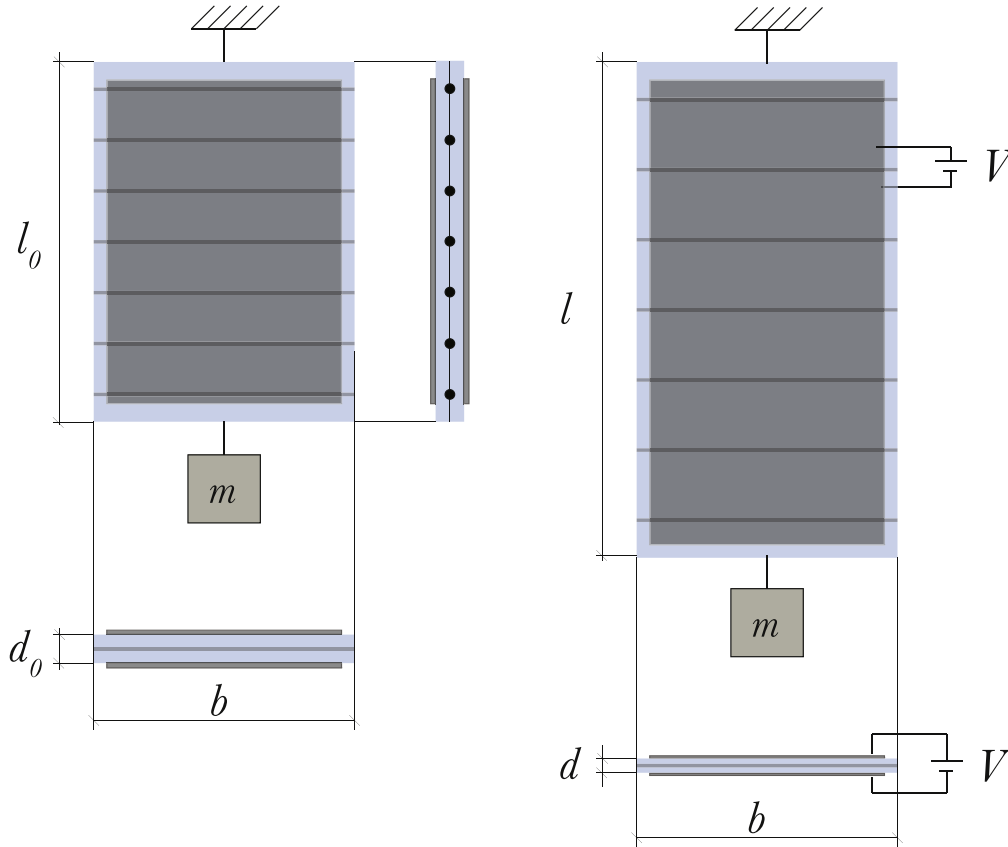
Figure 2. Schematic drawing of the DEA with embedded stiffening elements aligned along the transversal direction. When a load, schematically represented by the weight of a mass m, pre-stretches the actuator, the initial length l_0 is obtained (left). Upon application of a driving voltage V and since the elongation along the other in-plane direction is prevented by the stiffening elements (therefore the transversal dimension b does not change), the actuator elongates only along the longitudinal direction reaching the length $l > l_0$ and the thickness $d < d_0$.

0.125 mm in the regions between the stiffening elements. The use of that pre-strain is justified by its well-known beneficial effect in terms of increase of electromechanical actuation [19]. The stiffening elements, consisting of wood sticks of 1.5 mm in diameter and 50 mm in length, were aligned with a uniform pitch of 10 mm. The well-known adhesive properties of the VHB material simplified the manufacturing process by ensuring a proper bonding between the layers, also allowing for properly retaining the stiffening elements enclosed between them as schematically represented in figure 2. The DEA was eventually removed from the support frames and coupled with the plastic beam as better explained in the following. The compliant electrodes consisted of carbon conductive grease (MG Chemicals, Canada). The mass of the actuator, measured with a precision scale, accounted for 2.5 g. A schematic of the DE actuator is represented in figure 2.

In order to measure the axial stiffness of the DEA about the pre-stretched configuration, a set of three tensile tests with a uniaxial tensile machine was performed with two-hour interval between subsequent experiments to allow the recovery of viscoelastic strains. In each test, the DEA was secured to the load cell clamps with an initial length correspondent to the original strain of 300% along the longitudinal direction. The tests were performed with a speed
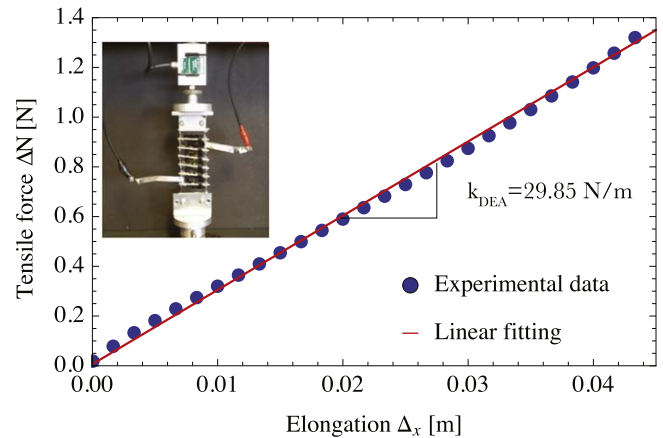

Figure 3. Tensile tests of the DEA to calculate the tensile stiffness $k_{\mathrm{DEA}} = 29.85$ N m^{-1} (performed with a strain rate of 0.043 s^{-1}). The average between three experiments are reported. The standard deviation is within the size of the point used to represent the data.

of 3 mm s^{-1} (corresponding to a strain rate of 0.043 s^{-1}). Results are shown in figure 3, in which the increment in force required to elongate the specimen is reported.

By noting that the linear fit indicated with a red line interpolates satisfactorily the experimental data, we computed
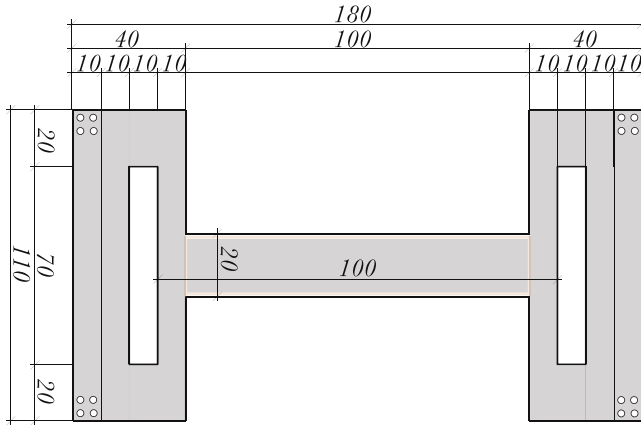
Figure 4. Schematic drawing of the plastic beam of the robot. All dimensions are expressed in mm.

Figure 5. Tensile test of the styrene plastic material: experimental stress–strain data and estimation of the Young's modulus.

its slope that corresponds to the stiffness of the specimen, namely $k_{DEA} = 29.85 \, \text{N m}^{-1}$.

The reproduction of the same test with a hyper-electro-elastic model has proven to be difficult due to the lack of reliable and extensive investigations of the behaviour of the acrylic elastomer under investigation at large in-plane pre-stretches. The work by Hossain *et al* [19] aimed at filling this gap, however the studied transverse pre-stretch was only up to 200%.

2.2.2. Plastic beam. The plastic beam of the robot was obtained from a 1.5 mm thick flat sheet of solid polystyrene plastic having a volumetric mass density of 1050 kg m^{-3}, the shape schematically represented in figure 4 was realized with a Computer Numerical Control (CNC) milling machine. The beam features a central part having a width of 20 mm and a length of 100 mm and two side appendices where, by exploiting the presence of interlocking holes (having a 2.5 mm diameter and 7 mm pitch), the clawed pads are secured. A rectangular opening on each appendix allowed for coupling the DEA to the plastic structure. The DEA was secured to the structure by means of one rigid plastic bar per side screwed to the structure as previously shown in figure 1. Each rigid plastic bar and its screws accounted for a weight of 1.25 g.

The polystyrene plastic was characterised by performing a tensile test with a uniaxial tensile machine on five 'dogbone' specimens conforming to the type V shape reported in the ASTM D638-03. The test speed was 0.0167 mm s^{-1}. From the average values of the experimental data reported in figure 5 we see that the stress–strain curve begins with a toe region. As stated in the Annex A1 to the ASTM D638-03, this region does not represent a property of the material since it is caused by a take up of slack and alignment or seating of the specimen. Therefore, to obtain a correct value of the elastic modulus, the stress–strain values must be compensated to give the corrected zero point on the strain or extension axis by following the reported procedure. According to such procedure, the modulus of elasticity is obtained by extending
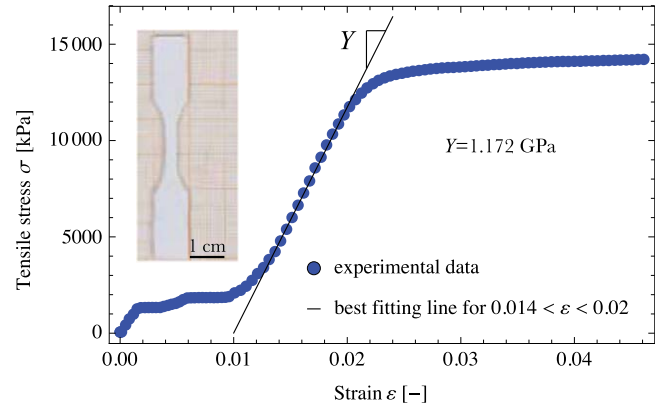
the initial linear portion of the load-extension curve and dividing the difference in stress corresponding to any segment of section on this straight line by the corresponding difference in strain using the average original area of the cross section in the gauge length segment of the specimen. Following this procedure for the strain interval $0.014 < \varepsilon < 0.02$, the Young's modulus $Y = 1.172 \, \text{GPa}$ was calculated.

2.2.3. Bristle pads. Two different types of bristle pads were tested. The first one was obtained by 3D printing a photopolymer resin (Clear FLGPCL02, FormLabs, USA) with a stereolithography 3D printer (Form2, FormLabs, USA) eventually exposed to UV rays for 20 min in order to increase its hardness. The second one consisted of stainless-steel bristles obtained from a commercial bristle belt used in the textile industry for carding fibres. Figure 6 shows a picture of each pad.

As shown in figure 6(a), the bristles of the 3D printed pads were manufactured with six different angles with respect to the vertical axis (from 15° to 65°). Despite the change of the angle, each pad featured a constant height of 6 mm, achieved by compensating the thickness of each base. Each pad presented a total of 49 bristles arranged in seven rows and seven lines aligned with a uniform pitch of 1.5 mm on a squared base plate having a 16 mm side dimension. Each bristle had a diameter of 0.7 mm ending with a sharp tip printed with convergent semi-angle of 13°.

The stainless-steel pads were composed of six rows and seven lines of bristles, aligned with a uniform pitch of 1.5 mm, for a total of 42 steel bristles on each pad. Each bristle possesses a 5 mm straight part coming out from the rubber substrate and an oblique part ending with a sharp tip also measuring 5 mm in length. As shown in figure 6(b), the oblique part presented an angle of 55° with respect to the vertical axis for a total height of 11 mm.

As better described in the following, during the locomotion tests of the robot both types of pads operated in contact with a horizontal surface covered with baking paper. For this reason, we measured the static friction coefficient
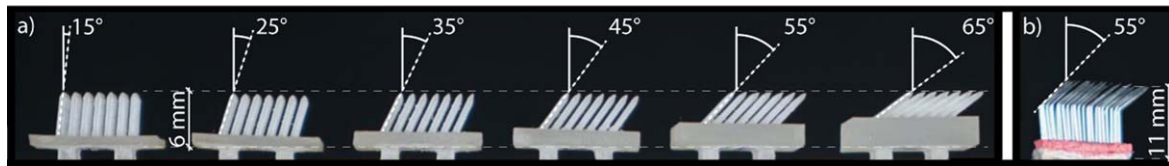
Figure 6. Bristle pads: resin 3D printed (a), stainless steel (b).

against baking paper of each pad either in the case of forward or backward sliding with an *ad hoc* custom-built setup, shown in figure 7.

The setup consisted of three main components: a tensile testing machine, a linear guide and a slider (figure 7). The linear guide was made out of rigid polycarbonate, whose top surface was coupled with a baking paper layer by means of double-sided adhesive tape, constituting the reference surface on which the samples were tested. The sample holder, coupled with the different samples of the bristle pads, constituted the slider, as shown in the close-up view of figure 7. The sample holder, whose self-weight corresponded to 7 g, also allowed for loading the sample with a supplementary mass $m = 20$ g, needed to maintaining a proper contact with the surface of the linear guide during the sliding. A double inextensible wire, connected to the grip of the tensile machine, pulled the slider with a constant speed of 0.1 mm s^{-1}. For each sample, the pulling force, i.e. the friction force transmitted from the sliding surface to the load cell trough a frictionless roller, was continuously recorded during the sliding. The self-weight of each 3D printed bristle pad was measured with a precision scale, the following values were recorded: 0.46 g, 0.51 g, 0.60 g, 0.74 g, 0.93 g and 1.18 g for angles 15°, 25°, 35°, 45°, 55°, 65°, respectively. The self-weight of the steel bristle pad accounted for 0.5 g. The total weight of the slider was calculated by adding the masses of the bristle pad, the sample holder and the supplementary mass m, allowing for calculating the total normal force applied to the sample for each test performed.

At the time of incipient sliding, when the detachment force was reached, the static friction force corresponded to the first maximum peak in the load-displacement curve. After reaching this peak, the sample started sliding at an approximately constant force value, corresponding to the dynamic friction force. When this value had stabilized, the test was stopped. The dynamic friction force was taken as the mean value during the sliding phase. Since no adhesion occurred, both the static and dynamic friction coefficients μ_s and μ_d were calculated as the ratio between the friction force (static and dynamic, respectively) and the applied normal load.

In figure 8, we report the experimental results obtained from the friction tests for every pad configuration. From the results, it can be deduced that while the 3D printed pads at first sight seems to be characterized by a similar behaviour in either forward or backward sliding, stainless steel pads exhibit a substantial variation in the coefficient of friction with respect to the sliding direction.

It is worth to point out that the friction coefficient for the 3D printed pads present variability related to the bristle's
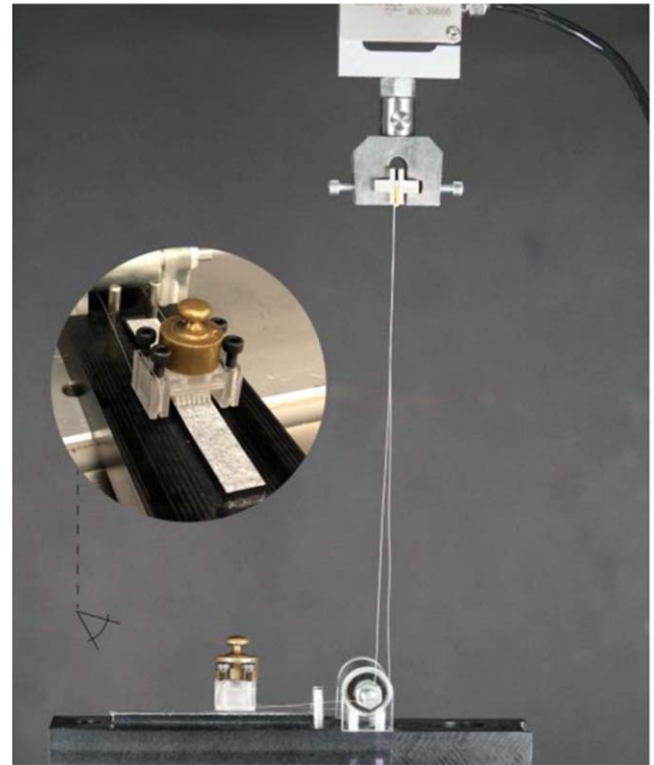

Figure 7. Experimental setup for the measurement of the friction force generated at the interface between the testing surface and the bristle pads. The bristle pad sample coupled to the sample holder and loaded with a mass $m = 20$ g constituting the slider. A double inextensible wire allowed for pulling the slider with a tensile machine along the linear guide covered with a layer of baking paper showed in the enlargement of the picture.

angle. Indeed, from figure 9 we see that both μ_s and μ_d peaks at 35° in case of backward sliding, while it seems that the optimum value for those coefficients in case of forward sliding lies within the range 35°−45°. The relatively high value of the friction coefficient for the pad whose angle is 15° can be explained considering that the bristles may have engaged with the baking paper surface during the sliding test. For such a low value of the angle the entire load was applied directly to the bristle tip, possibly inducing a slight indentation.

As shown in figure 8 and highlighted in figure 10, for the 3D printed pads with a grade up to 35° the friction coefficient measured during the backward sliding was greater than that observed during the forward sliding. Conversely, when the value of the angle increased beyond 35°, an opposite trend was revealed. This trend may lead to the possibility of a motion inversion of the robot simply triggered by a variation of its actuation frequency.
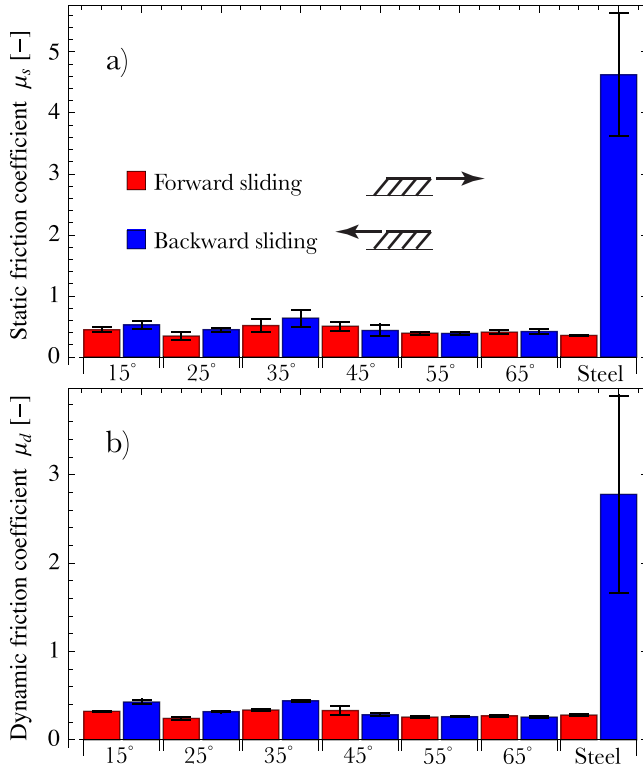
Figure 8. Static (a) and dynamic (b) friction coefficients of the six 3D printed bristle pads (indicated with the values of the angles) and the steel bristle pad.

This behaviour has been already revealed in a bristle-bot featured by flexible joints between the bristles and the substrate [20, 21]. The one we present here possesses rigid bristles. We do believe this is the reason why we were not able to observe such motion inversion during the locomotion tests we performed. Nonetheless, we also believe that a motion inversion is possible by optimizing the bristle's design.

2.3. Robot manufacturing

Upon coupling with the plastic beam, the DEA was subject to a tensile load along the longitudinal direction. Due to the highly viscoelastic behaviour of the VHB acrylic elastomer, its length increased from 70 to 110 mm after 24 h, resulting in an increase of its longitudinal pre-stretch from the initial 300% up to 529%. This caused a further average thickness reduction of the DE membrane from 0.125 to 0.080 mm, calculated assuming material incompressibility. As better described in the following, during the locomotion tests the robot was eventually loaded on its top with a lumped mass $m = 9$ g made out of two metallic bolts coupled together by means of a double-sided adhesive tape of negligible weight.

2.4. Estimation of the fundamental frequency

The analysis of the locomotion of the robot requires the estimate of the fundamental frequency f_n of the system that is computed in this section following two approaches: the one that is first presented is based on the Rayleigh's quotient method, the second one relies on a finite element computation.

2.4.1. Analytical: Rayleigh's quotient method. The fundamental frequency of the robot is estimated through the Rayleigh's quotient [22] on the structure schematically represented in figure 11. In this calculation, the asymmetry induced by the bristles is neglected and therefore the structure is considered symmetric and only its left-hand half is studied, being composed of six sub-systems, namely the beam segment EF, the parts AB, BD and DE, the spring DO and the lumped mass $m/2$. Slider constraints are imposed along the symmetry axis y in F and O.

The horizontal length $l/2 = 55$ mm and the height $h = 25$ mm correspond to the half-length of the dielectric elastomer actuator and to the rise of the beam in the operational configuration, respectively. The curved beam DFD' can be satisfactorily described by the sinusoidal function

$$y(x) = h\left[\sin\left(\left(x + \frac{l}{2}\right)\frac{\pi}{l}\right)\right] \tag{1}$$

and its slope in D, namely $y'(-l/2)$, provides the angle $\bar{\theta}$.

When the square wave voltage signal is applied to the elastomer actuator, the structure of the robot vibrates around its initial configuration with the fundamental mode sketched in figure 12. We assume that during this motion, the parts AB and BD undergo a rigid rotation about point D as represented in the detail of figure 12. By considering the static scheme of the beam shown in figures 11 and 12, with an application of the principle of the virtual work (see appendix) it is possible to calculate that an arbitrary horizontal infinitesimal displacement δ_x in D generates a vertical displacement in F whose value is $1.772\,\delta_x$. With reference to figure 11, we introduce the curvilinear abscissa s on the beam segment DF, and the coordinates η and ξ on AB and BD, respectively. The displacements of the actuator DO is described by the coordinate x.

When the system is vibrating in its fundamental eigenmode, by assuming a separable solution for the generic displacement $\boldsymbol{w}$ of its points, for each component of the system we can formally write

$$\boldsymbol{w}(\psi, t) = \boldsymbol{W}(\psi)\sin(\omega_n t) = (w_x(\psi)\boldsymbol{i} + w_y(\psi)\boldsymbol{j})\sin(\omega_n t), \tag{2}$$

where $\boldsymbol{W}(\psi)$ is an eigenfunction that approximately represents the shape of the system and ω_n is the vibration circular frequency. In equation (2), ψ represents the generic abscissa describing each element of the structure and $\boldsymbol{i}$ and $\boldsymbol{j}$ are the component of an orthonormal basis associated with axis x and y, respectively. In particular, $\psi \equiv s$ for the segments DE and EF, $\psi \equiv \eta$ for AB, $\psi \equiv \xi$ for the segment BD and $\psi \equiv x$ for the spring DO. The vertical displacement of mass $m/2$ corresponds to the same quantity of the beam segment EF at point F.

The Rayleigh's quotient allows the evaluation of the frequency $f_n = \omega_n/2\pi$ by equalling maximum strain ($U^{\max}$) and maximum kinetic ($K^{\max}$) energies computed for the system by assuming the vibration mode described by
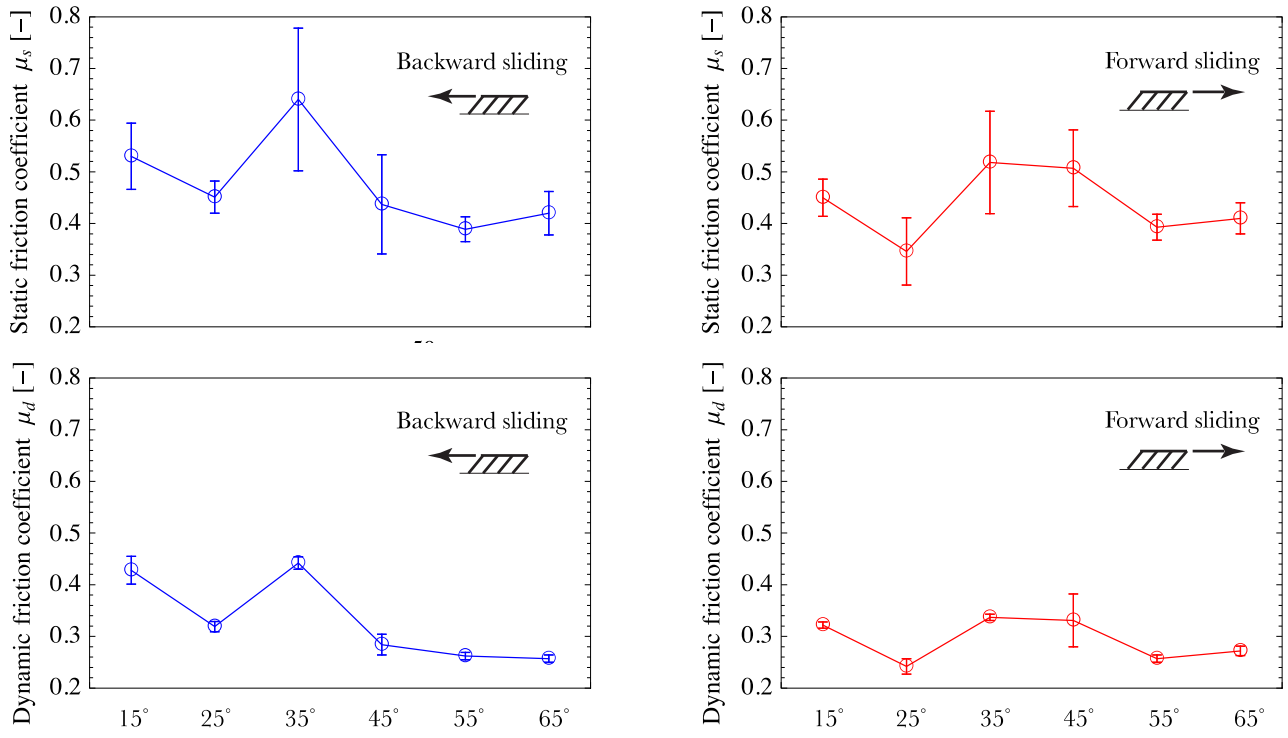
Figure 9. Static and dynamic friction coefficients of the 3D printed bristle pads for increasing value of the bristle's angle.
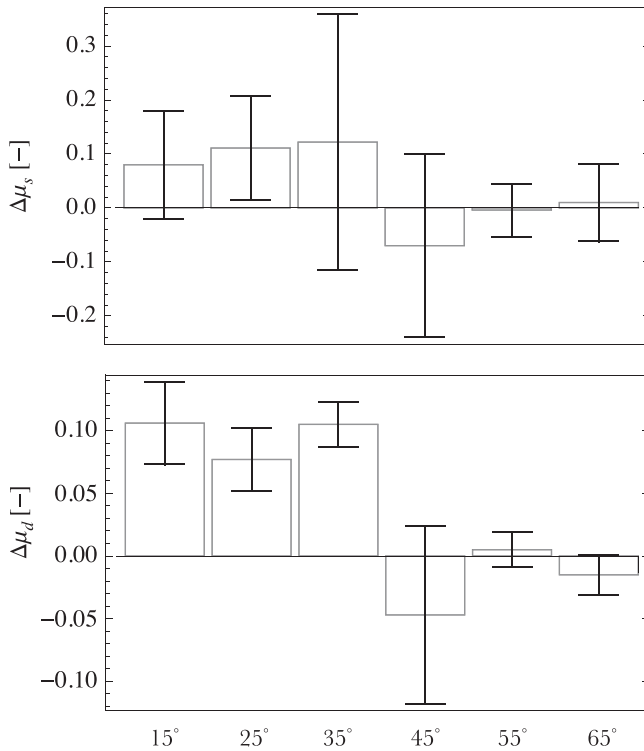

Figure 10. Variation of the backward versus forward sliding static and dynamic friction coefficients of the 3D printed bristle pads for increasing value of the bristle's angle. The error bar associated with each value of $\Delta\mu_s$ and $\Delta\mu_d$ is calculated according to the variance sum law.
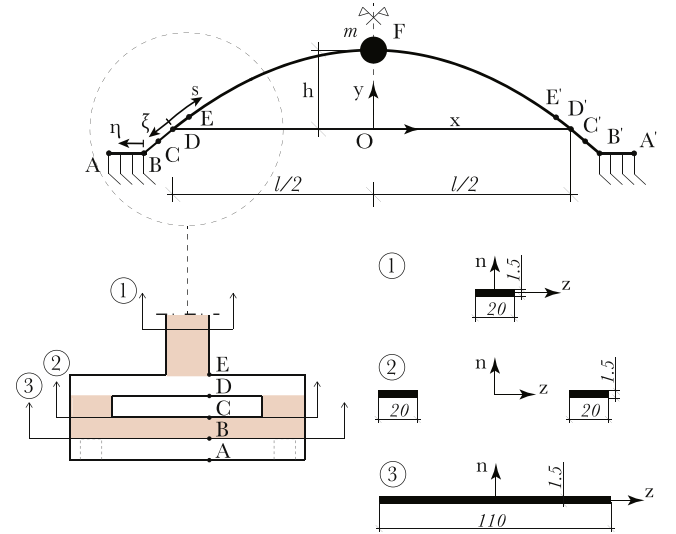

Figure 11. Schematic representation of the robot structure. Top: longitudinal section. Bottom: top view of the detail of the connection between curved beam, straight actuator and clawed pads (whose perimeters are sketched with dashed lines) (left) and detail of the cross sections (right). Coordinate z describes the out-of-plane axis. Dimensions are expressed in mm.

equation (2), namely

$$\sum_{i=1}^{6} U_i^{\max} = \sum_{i=1}^{6} K_i^{\max}, \qquad (3)$$

where the two energies are written as a sum of contributions of the six subsystems, each described by index i running from
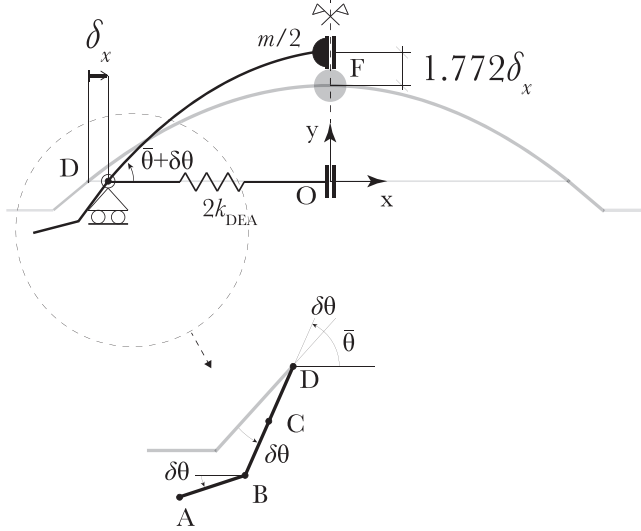
Figure 12. Schematic representation of the robot about the initial configuration of equilibrium. An imposed horizontal displacement δ_x in D induces a vertical displacement $1.772\,\delta_x$ in F. The magnification shows the kinematics of the rigid motion of the structure about point D.

1 to 6, as detailed in the following. Note, however, that for some elements the maximum strain energy is vanishing. It should be emphasised that due to the form (2) of the eigenmode, in the interval $t \in [0, 2\pi/\omega_n[$ the maximum strain energy for each element is reached at $t = \pi/(2\omega_n)$, while the maximum kinetic energy is to be sought at $t = 0$.

Beam EF ($i = 1$). For the beam segment EF, we assume that its shape during the vibration is described by the shape function $\boldsymbol{W}(s) = w_x(s)\boldsymbol{i} + w_y(s)\boldsymbol{j}$ whose components are

$$w_x(s) = \delta_x \cos\left(\pi\frac{s}{L}\right), \tag{4a}$$

$$w_y(s) = 1.772\,\delta_x \sin\left(\pi\frac{s}{L}\right), \tag{4b}$$

where $L = 120$ mm. The kinetic energy is therefore given by

$$K_1 = \frac{1}{2}\int_{L/12}^{L/2} \mu_1 \dot{w}(s, t)^2 ds, \tag{5}$$

where the mass per unit length $\mu_1 = 0.0315\,\text{kg m}^{-1}$ is calculated over a length of 0.05 m (that corresponds to the half-length of the central beam as shown in figure 4) and a superposed dot indicates differentiation with respect to time. The transverse component of the total displacement, which is the one contributing to the elastic strain energy when the axial elongation of the beam is neglected, is given by

$$\boldsymbol{w}_{\text{tr}}(s, t) = \boldsymbol{w}(s, t)\cos\gamma(s), \tag{6}$$

where $\gamma = \pi/2 - \alpha + \beta$, with $\alpha = \tan^{-1}(y'(x))$ and $\beta = \tan^{-1}(w_x(s)/w_y(s))$. The strain energy stored during the deformation is

$$U_1 = \frac{1}{2}YI_{zz}\int_{L/12}^{L/2} (\boldsymbol{w}_{\text{tr}}(s, t)'')^2 ds, \tag{7}$$

where I_{zz} is the second moment of area of the beam cross section (see figure 11) and a dash denote differentiation with respect to the coordinate s.

Beam DE ($i = 2$). The shape of the beam segment DE is also described by the shape function $\boldsymbol{W}(s)$ defined through the components (4). Assuming that the section vibrates as a rigid body, the strain energy is $U_2 = 0$, whereas the kinetic energy can be written as

$$K_2 = \frac{1}{2}\int_0^{L/12} \mu_2 \dot{w}(s, t)^2 ds, \tag{8}$$

where the mass per unit length $\mu_2 = 0.2983\,\text{kg m}^{-1}$ is calculated taking into account the weights of both the plastic structure between points D and E (figure 11) and the rigid plastic bar screwed on it.

Segment AB ($i = 3$). This is a rigid body, therefore $U_3 = 0$. Considering a uniform mass distributed along AB whose density (per unit length) is $\mu_3 = 0.273\,\text{kg m}^{-1}$ (μ_3 is comprehensive of the two bristle pads each weighing 0.5 g), the kinetic energy of AB is given by

$$K_3 = \frac{1}{2}\int_0^{\overline{\eta}} \mu_3 \dot{w}(\eta, t)^2 d\eta, \tag{9}$$

where the components of the displacement along x and y are

$$w_x(\eta) = \delta_x + \overline{\xi}\,\delta\theta\sin\overline{\theta}, \tag{10a}$$

$$w_y(\eta) = -\overline{\xi}\,\delta\theta\cos\overline{\theta} - \eta\,\delta\theta, \tag{10b}$$

respectively.

Segment BD ($i = 4$). BD is considered as a rigid body as well, then $U_4 = 0$. Considering a uniform mass distribution $\mu_4 = 0.1181\,\text{kg m}^{-1}$, the kinetic energy of BD can be written as

$$K_4 = \frac{1}{2}\int_0^{\overline{\xi}} \mu_4 \dot{w}(\xi, t)^2 d\xi, \tag{11}$$

where the components of the displacement along x and y are now given by

$$w_x(\xi) = \delta_x + \overline{\xi}\,\delta\theta\sin\overline{\theta}, \tag{12a}$$

$$w_y(\xi) = -\overline{\xi}\,\delta\theta\cos\overline{\theta}. \tag{12b}$$

Dielectric elastomer actuator ($i = 5$). The DE actuator is modelled as a spring of length $l/2$, therefore the stiffness is twice that computed in section 2.2.1, namely $2k_{\text{DEA}} = 59.70\,\text{N m}^{-1}$. Moreover, $\mu_5 = 0.0227\,\text{kg m}^{-1}$ and the two components of the displacement function are

$$w_x(x) = -\delta_x\left(\frac{2x}{l}\right), \tag{13a}$$

$$w_y(\eta) = 0. \tag{13b}$$

Therefore, the kinetic energy is

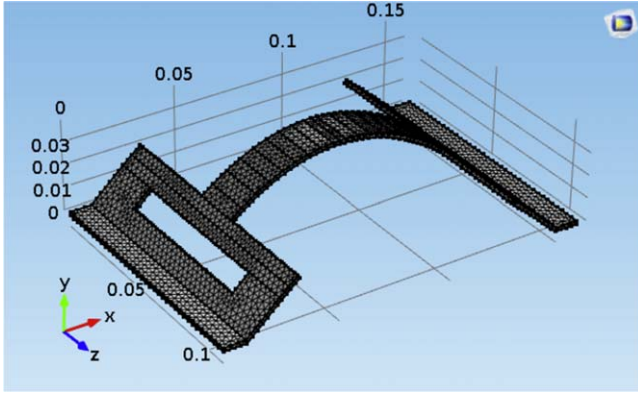$$K_5 = \frac{1}{2}\int_{-l/2}^{0} \mu_5 \dot{w}(x, t)^2 dx, \tag{14}$$

Figure 13. Mesh of the robot plastic structure about the initial configuration of equilibrium. The DEA is not visually represented since its presence is imposed as equivalent spring constraints to the plastic structure.

while the maximum value of the strain energy can be easily written as

$$U_5^{\max} = \frac{1}{2}(2k_{\text{DEA}})\delta_x{}^2. \tag{15}$$

Point mass ($i = 6$). The mass possesses only kinetic energy (i.e. $U_6 = 0$) that can be written as

$$K_6 = \frac{m}{4}(\dot{w}_y(s)|_{L/2})^2. \tag{16}$$

Equation (3) can be solved for ω_n to obtain the estimation of the fundamental frequency f_n. The values $f_n = 24.29\,\text{Hz}$ and $f_n = 19.77\,\text{Hz}$ were calculated for $m = 0$ and $m = 9\,\text{g}$, respectively.

2.4.2. Numerical: finite element analysis. The finite element method (FEM) was used to numerically estimate the eigenfrequencies and the modal shapes of a 3D model of the robot. The model was developed with the Solid Mechanics module of the COMSOL Multiphysics v. 5.0 software. In this model, the polystyrene plastic beam was considered as a linear elastic material. While the Young's modulus Y was obtained with the tensile test reported in section 2.2.2, the value of the Poisson's ratio $\nu = 0.32$ was adopted from literature [23]. We exploit the symmetry of the structure by imposing a null displacement of the centreline in F along x and z, and a roller constraint along both the edges in D and D' which corresponds to the static scheme reported in section 2.4.1. We assume that the shape of the central beam in the deformed configuration is given by (1) while all the other dimensions are as reported in figure 4. The lumped mass m and the masses due to the bristle pads, to the rigid bar and its screws and the mass of the DEA are assigned as edge loads along the edges defined by the points F, A, E and D, respectively. The DEA is modelled as a linear spring by assigning a 'Spring Foundation' constraint with $2k_{\text{DEA}} = 59.70\,\text{N m}^{-1}$ in correspondence of each roller. The structure was meshed with 9167, 6738, 1410 and 132 tetrahedral,
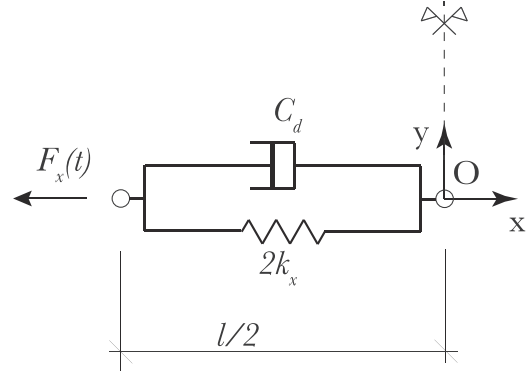

Figure 14. Kelvin–Voigt model adopted to describe the viscoelastic behaviour of the DEA.

triangular, edge and vertex quadratic elements respectively by using the COMSOL mesh subroutine. The meshed structure is shown in figure 13. The eigenfrequencies and the correspondent modal shapes, for both the loaded with $m = 9\,\text{g}$ and the unloaded case, were obtained by using the COMSOL's 'Eigenfrequency Study' solver. The values $f_n = 22.79\,\text{Hz}$ and $f_n = 18.12\,\text{Hz}$ were calculated for $m = 0$ and $m = 9\,\text{g}$, respectively.

2.5. Frequency response analysis: calculation of net displacement and locomotion speed

In this section, we report about the FEM model developed to calculate the overall net displacement of the robot δ_x during each actuation cycle as a function of the actuation frequency f. To do so we modified the numerical model presented in section 2.4.2 by taking in account the viscoelastic response of the DE actuator, as better explained in the following of this section. This allowed the theoretical locomotion speed along the x-axis v_x, namely

$$v_x = f\,\delta_x, \tag{17}$$

to be estimated and compared with the experimental measurements.

The structure was loaded with a force F_x, applied as a step load in correspondence of the external edge identified on the plastic structure by the point D (see figure 11) with frequency f to simulate the effect of the voltage driving. The force was set to $F_x = 0.25\,\text{N}$ since for this value the total displacement δ_x obtained from the model with a static analysis was equal to that measured in the lab, namely $\delta_x = 1\,\text{mm}$.

The frequency response of the robot highly depends on the mechanical damping of its deformable components: the polystyrene plastic beam and the VHB 4910 DE actuator. The damping of the polystyrene plastic beam was modelled with a rate-independent isotropic structural loss factor $\eta = 0.04$ [24], which is defined as the ratio of the energy dissipated per cycle to the maximum strain energy stored. The frequency response of the DEA requires a more accurate modelling due to its highly frequency-dependent viscoelastic behaviour [25]. For this reason, we modelled it as a Kelvin–Voigt material, which consists of a purely viscous damper and a purely elastic spring connected in parallel [26] as shown in figure 14.

For this model, the relaxation time constant τ is

$$\tau = \frac{C_d}{2k_x},\tag{18}$$

where C_d is the coefficient of viscous damping and $2k_{\mathrm{x}}$ is the stiffness of the VHB material.

Since the elastomer is loaded with a time-dependent load, it presents a rate-dependent viscoelastic behaviour that results in a reduction of the relaxation time constant τ for increasing values of the longitudinal stretch rate $d\lambda/dt$. In particular, by assuming the nonlinear nonaffine model presented in [27], we find that such relation monotonically decreases for increasing stretch rates with the law

$$\tau = A\left(\frac{d\lambda}{dt}\right)^{-B},\tag{19}$$

where $A = 2.94\ \mathrm{s}^{1-B}$, $B = 1.12$ and $d\lambda/dt$ is the stretch rate of the elastomer (response) that we assume being coincident with the frequency f (stimulus) of the voltage input of the DEA during each actuation cycle between the range $1 \leqslant f \leqslant 30$ Hz. By equating (18) and (19) we get the expression of coefficient C_d as a function of the frequency f, namely

$$C_d = 2k_x\, A\left(\frac{d\lambda}{dt}\right)^{-B}.\tag{20}$$

It is worth to point out that the model leading to equation (19) is validated [27] with an experimental investigation performed on VHB specimens longitudinally pre-stretched up to 6 times their initial length, for frequencies spanning over four orders of magnitude ($6.7 \cdot 10^{-5} - 0.67$ Hz). In our case we have a biaxial stress state with a similar longitudinal stretch but also a transverse stretch and higher actuation frequencies. However, despite these discrepancies, due to the lack of both experimental data and models available in literature, by taking into account higher frequencies and biaxial stretch states, we adopt this model to describe the behaviour of our DE actuator, although a certain grade of approximation might be introduced.

The model was analysed with the COMSOL's 'Frequency Domain Study' solver in the range of frequencies investigated in the experiments allowing for obtaining the frequency dependent displacements of the structure reported in section 3. The chosen frequency step was $\Delta f = 0.1$ Hz.

2.6. Locomotion test: experimental setup and test procedure

The experimental setup here described was conceived to measure the locomotion speed of the robot as a function of the actuation frequency of the DE actuator. In this regard, a 0.3 m long testing track consisting of a flat surface coated by a thin sheet of baking paper to achieve homogeneous roughness was used as a surface course. A laser optical transducer (optoNCDT, Micro-Epsilon, USA) was used as finish line, while a high-voltage amplifier (Model 10/10B, Trek Inc., USA) provided the driving voltage. The generator was connected to the electrodes of the DEA by means of two thin metal stripes and thin wires to avoid any constraint during the locomotion. A square wave voltage signal V, with 6 kV of
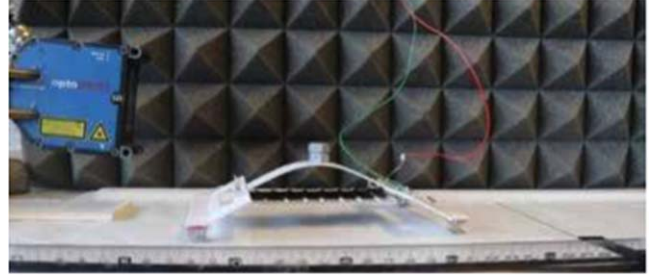

Figure 15. Picture of the experimental setup.

amplitude, was provided to the DEA with frequencies within the range 5–30 Hz. A custom made LabView program allowed for simultaneously applying the driving voltage to the DE actuator (thus triggering the locomotion of the robot) and record the time of its application. Both the voltage and the time counter were automatically switched off when the robot reached the vertical laser beam located at the end of the testing track. For each frequency tested, the average locomotion speed of the robot was obtained by measuring the time needed to complete the full length of the testing track. Each locomotion test was repeated five times, allowing for obtaining the experimental speed values in terms of mean and standard deviation. Figure 15 shows a picture of the experimental setup used for the tests.

3. Results and discussion

The locomotion tests revealed that a forward displacement δ_x was observed only when the robot was equipped with the steel bristle pads. Conversely, a vibration about the starting position, with no net displacement, was recorded when the robot was equipped with the 3D printed bristles for any whole frequency in the range 5–30 Hz. This evidence suggests that the magnitude of the frictional anisotropy generated by the robot's bristles plays a key role for achieving a forward motion. Indeed, as shown in figure 8, the 3D printed bristles featured a much smaller frictional anisotropy compared to the steel ones; this result justifies the inability of the robot to advance on the surface chosen for the experiments. The experimental values of the locomotion speed measured during the tests performed with the steel bristles are shown with blue circles in figure 16.

In particular, figure 16 (bottom) reports the locomotion speed measured for the robot loaded with a lumped mass $m = 9$ g whereas figure 16 (top) shows the results for the case of unloaded robot. We observe that the locomotion speed increased in both cases up to a maximum value, namely $3.0\ \mathrm{cm\,s}^{-1}$ at an actuation frequency of 19 Hz in the former case and $4.7\ \mathrm{cm\,s}^{-1}$ at $f = 23$ Hz in the latter. The two vertical dotted lines drawn in each graph mark the fundamental frequencies f_n estimated with the two methods described in section 2.4.

The data reported figure 16 show that for both the cases of unloaded and loaded robot, the maximum value of the
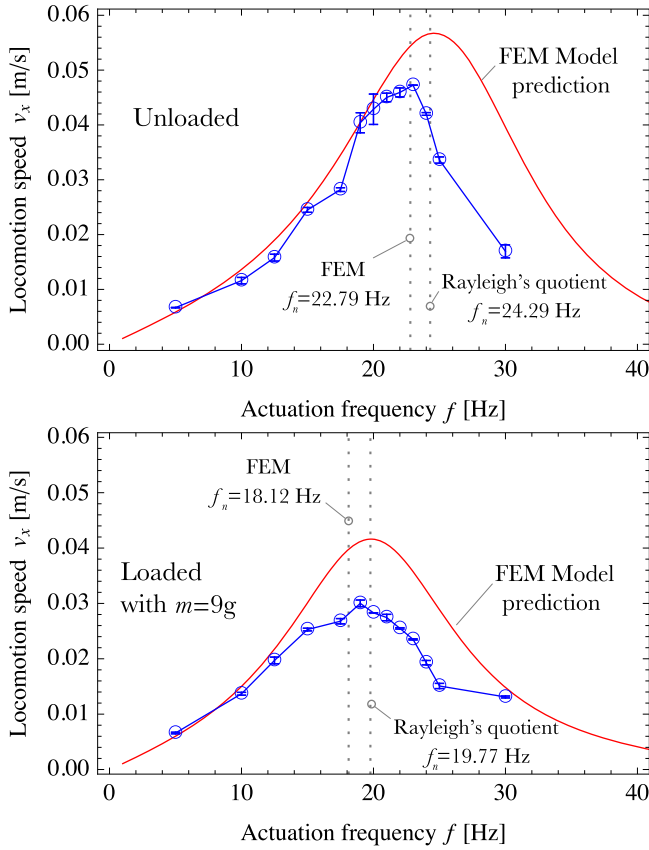
Figure 16. Locomotion speed v_x versus actuation frequency f: experimental data and model prediction for the unloaded (top) and loaded with $m = 9$ g (bottom) robot. Bars represent the standard deviation of measures. The two dotted lines represent the fundamental frequency f_n calculated with either the Rayleigh's quotient method (on the right in both plots) or the FEM modal analysis (on the left in both plots).

experimental locomotion speed lies within the range of fundamental frequencies calculated with the two proposed methods. In particular, the Rayleigh's quotient method gives an upper-bound estimate of f_n whereas the FEM calculations provide values that are approximately 6.5% and 9.5% lower with respect to the former for the unloaded and the loaded robot, respectively. From the superposition between the experimental data and the locomotion speed model predictions, calculated with the FEM frequency response analysis described in section 2.5, we see that the model predicts a rising locomotion speed up approximately to the fundamental frequency. For higher values of the frequency f, the model foresees lower values of the speed v_x in a fairly good agreement with the experimental data. In the absence of any damping mechanism or constrain, we would have theoretically expected an unbounded, asymptotic behaviour for the locomotion speed at the fundamental frequency f_n computed via FEM (indicated with 'FEM' in figure 16), that also represents the resonance frequency for the system. In the current framework, the peak of the locomotion speed is slightly shifted to the right with respect to f_n as, in

equation (17), the displacement is multiplied by the frequency f itself.

The behaviour highlighted in the previous paragraph can be explained by considering that the frequency response of the robot is given by a combination of its eigenmodes. Indeed, for increasing value of the actuation frequency from zero to the first eigenvalue, the structure would tend to vibrate according to the first eigenmode, as represented in figure 17 (top). Since the first eigenmode is symmetric, the net displacement δ_x is given by the sum of two components that are equal in modulus. Conversely, when the robot vibrates according the second eigenmode (shown in figure 17, bottom), which is asymmetric, the net displacement δ_x sharply decreases. This behaviour highlights the importance of identifying the correct value of the first eigenfrequency in order to maximise the locomotion speed.

As previously anticipated, the fundamental frequency f_n of the robot decreases at an increase of the weight of the lumped mass. Figure 18 shows the experimental data points correspondent to the value of f_n measured at the maximum locomotion speed (i.e. in correspondence with the natural vibration frequency) and the outcome of both FEM analysis (red solid line) and Rayleigh's quotient method (solid blue line), the former interpolating a finite number of points whose distance along the abscissa corresponds to $\Delta m = 0.1$ g. The agreement between tests and theory is very good.

Despite the inability of the 3D printed bristles to trigger locomotion for such low grade of frictional anisotropy, it is worth to point out that the effect of the bristle's angle on the actuation performance might be relevant when the frictional anisotropy reaches the threshold. Indeed, when a set of bristles reaches the frictional anisotropy threshold for locomotion, since the frictional anisotropy is null when both the back and front bristle's angle are either 0° or 90°, it must be that that for an intermediate value of the bristle's angle the frictional anisotropy is maximised.

In our case, from the friction measurements performed on the 3D printed bristles reported in figure 9, we see that both the static and dynamic friction coefficients peak for an angle of 35° for a backward sliding, while it seems that the maximum value is in the range 35°−45° when the sliding is forward. The relatively high value of friction observed for the angle whose value is 15° in both the backward and the forward sliding might be explained with the indentation occurred between the sharp tips and the paper, which is reasonable to observe for such a low value of the bristle's angle. Either the identification of the optimum value of such an angle to achieve the maximum locomotion speed or the investigation of other kind of bristles might be the goals of a future work.

4. Conclusions

In this paper, we have presented the concept of a novel kind of limbless resonating locomotion robot supported by four pads with asymmetric metallic rigid bristles. The forward
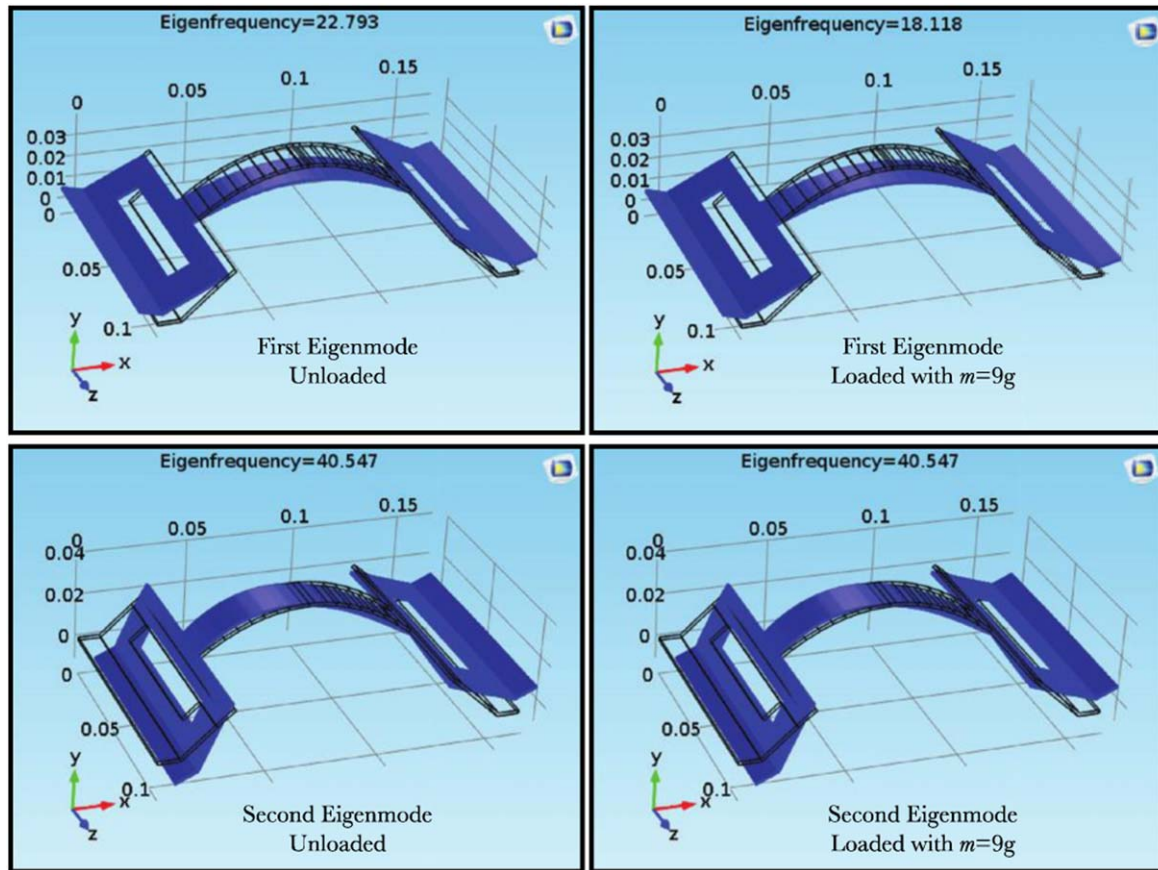
Figure 17. Eigenfrequencies and modal shapes of a 3D model of the robot: first vibration mode for the unloaded (top left) and loaded with $m = 9$ g (top right) robot; second vibration mode for the unloaded (bottom left) and loaded with $m = 9$ g (bottom right) robot.
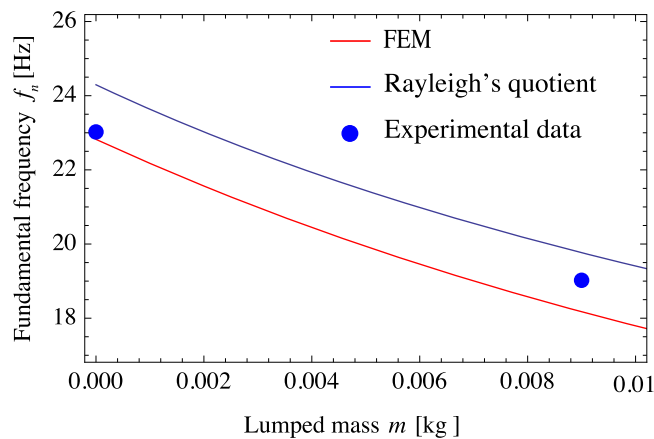

Figure 18. Fundamental frequency versus lumped mass weight. The experimental data corresponding to the peak values of the locomotion speed, namely 19 Hz for $m = 9$ g and 23 Hz for $m = 0$ are marked by dots. The blue solid line represents the predictions of the Rayleigh's quotient method whereas the red solid one refers to the FEM calculations performed with a step along the abscissa corresponding to $\Delta m = 0.1$ g.

motion of the robot was generated by the voltage-driven elongation of the dielectric elastomer actuator that triggers a partial release of the elastic energy stored in the plastic beam, enabling the stick-slip locomotion favoured by the frictional anisotropy of the pads. The locomotion speed reached a

maximum in the vicinity of the fundamental frequency of the system that was estimated either analytically or numerically. The behaviour of the robot was successfully captured by a numerical model where the damping characteristics of the elastomer were simulated with a Kelvin–Voigt rheological scheme.

We have also 3D-printed and tested similar robots equipped with resin pads with different bristle's angles. However, all those systems proved not to be able to display any forward motion. The reason is to be found in the lack of anisotropy of the friction coefficients for the pads.
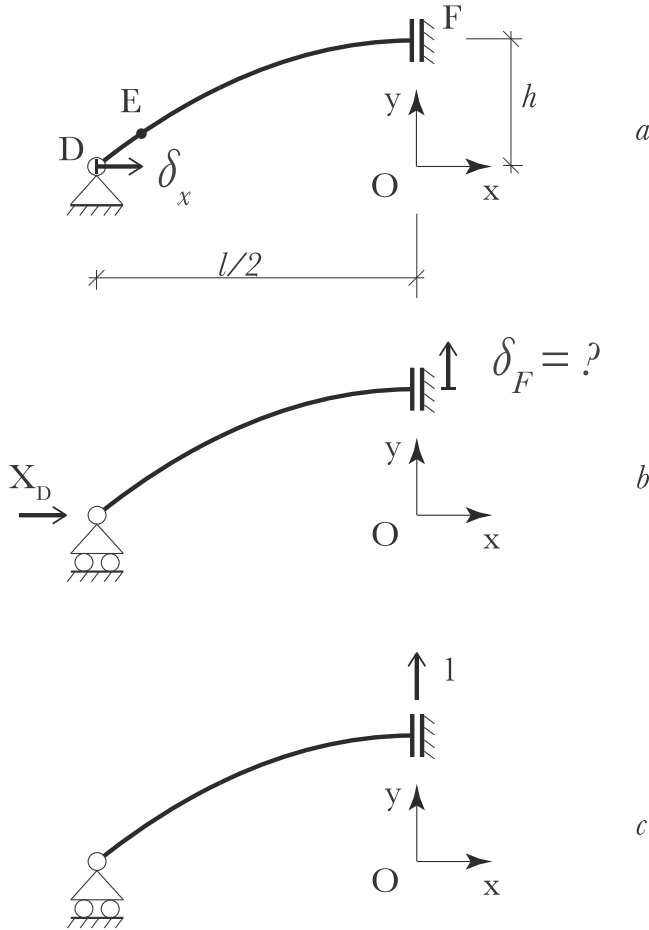
Acknowledgments

Figure A1. Static schemes adopted to calculate the vertical displacement δ_F: (a) one-time redundant structure subjected in D to a horizontal displacement δ_x; (b) statically-determined system employed to solve the structure in (a) through the second Castigliano's theorem (a); (c) statically-admissible auxiliary system for the application of the principle of virtual work to calculate δ_F.

Appendix

The vertical displacement in F (δ_F) of the structure displayed in figure 12 when the support D is subjected to a horizontal displacement δ_x can be computed in two steps: (i) the one-time redundant structure displayed in figure A1(a) is solved, in particular the horizontal reaction X_D is computed; (ii) the vertical displacement in F of the statically-determined scheme sketched in figure A1(b) is calculated. We refer to the coordinate system *Oxy* reported in figure 12 and to the function (1) for the shape of the arch. In addition, coherently with the assumption adopted in section 2.4.1, the segment DE of the beam is assumed to be rigid.

For the former problem, the second Castigliano's theorem can be invoked on the statically determined structure in figure A1(b), and by noting that the bending moment function is $M(x, X_D) = X_D\, y(x)$, the solving equation for X_D turns out to be

$$\delta_x = \int \frac{M}{YI_{zz}} \frac{\partial M}{\partial X_D} ds = \frac{X_D}{YI_{zz}} \int_{-cl}^{0} (y(x))^2 \sqrt{1 + (y'(x))^2}\, dx,$$

$$(A1)$$

where $-cl$ (with $c = 0.4255$) is the x-coordinate of point E. This leads to $X_D = YI_{zz}\, \delta_x/\Gamma$, where Γ is the value of the integral in equation (A1).

For the latter calculation, the principle of virtual work is applied by taking as a kinematical admissible scheme the real structure, i.e. that in figure A1(b), whereas as a statically admissible scheme (whose relevant quantities are denoted by *) the auxiliary one reported in figure A1(c) is adopted. In particular, by noting that $M^*(x) = x + l/2$, the displacement δ_F corresponds to

$$\delta_F = \int \frac{M\, M^*}{YI_{zz}} ds = \frac{X_D}{YI_{zz}} \int_{-cl}^{0} y(x)\left(x + \frac{l}{2}\right)$$
$$\times \sqrt{1 + (y'(x))^2}\, dx = 1.772\, \delta_x. \qquad (A2)$$

ORCID iDs

Luigi Calabrese ⓘ https://orcid.org/0000-0002-8276-7314
Massimiliano Gei ⓘ https://orcid.org/0000-0003-3869-7504
Nicola Maria Pugno ⓘ https://orcid.org/0000-0003-2136-2396

References

[1] Fu K, Moreno D, Yang M and Wood K L 2014 Bio-inspired design: an overview investigating open questions from the broader field of design-by-analogy *J. Mech. Des.* **136** 111102
[2] Holland O and McFarland D 2001 *Artificial Ethology* (New York: Oxford University Press)
[3] Langton C G (ed) 1997 Artificial life: an overiview *Complex Adaptive System* (Cambridge, MA: MIT Press)
[4] Meyer J A and Guillot A 2008 Biologically inspiered robots *Springer Handbook of Robotics* ed B Siciliano and O Khatib (Berlin: Springer)
[5] Kim S, Laschi C and Trimmer B 2013 Soft robotics: a bioinspired evolution in robotics *Trends Biotechnol.* **31** 287–94 Cell Press
[6] Dickinson M H, Farley C T, Full R J, Koehl M A R, Kram R and Lehman S 2000 How animals move: an integrative view *Science* **288** 100–6
[7] Duduta M, Clarke D R and Wood R J 2017 A high speed soft robot based on dielectric elastomer actuators *2017 IEEE Int. Conf. on Robotics and Automation (ICRA)* (Piscataway, NJ: IEEE) pp 4346–51
[8] Cao J, Liang W, Wang Y, Lee H P, Zhu J and Ren Q 2019 Control of a soft inchworm robot with environment adaptation *IEEE Trans. Ind. Electron.* (https://doi.org/10.1109/TIE.2019.2914619)
[9] Li T, Zou Z, Mao G, Yang X, Liang Y, Li C and Yang W 2019 Agile and resilient insect-scale robot *Soft Robot.* **6** 133–41
[10] Ahlborn B K, Blake R W and Megill W M 2006 Frequency tuning in animal locomotion *Zoology* **109** 43–53
[11] Filippov A and Gorb S N 2013 Frictional-anisotropy-based systems in biology: structural diversity and numerical model *Sci. Rep.* **3** 1240
[12] Tramsen H T, Gorb S N, Zhang H, Manoonpong P, Dai Z and Heepe L 2018 Inversion of friction anisotropy in a bio-inspired asymmetrically structured surface *J. R. Soc. Interface* **15** 20170629

[13] Carpi F, De Rossi D, Kornbluh R, Pelrine R and Sommer-Larsen P (ed) 2008 Dielectric elastomers as electromechanical transducers *Fundamentals, Materials, Devices, Models and Applications of an Emerging Electroactive Polymer Technology* (Oxford: Elsevier)

[14] Rosset S, O'Brien B M, Gisby T, Xu D, Shea H R and Anderson I A 2013 Self-sensing dielectric elastomer actuators in closed-loop operation *Smart Mater. Struct.* **22** 104018

[15] Dubois P, Rosset S, Niklaus M, Dadras M and Shea H 2008 Voltage control of the resonance frequency of dielectric electroactive polymer (DEAP) membranes *J. Microelectromech. Syst.* **17** 1072–81

[16] Pelrine R, Kornbluh R, Pei Q and Joseph J 2000 High-speed electrically actuated elastomers with strain greater than 100% *Science* **287** 836–9

[17] Lu T, Huang J, Jordi C, Kovacs G, Huang R, Clarke D R and Suo Z 2012 Dielectric elastomer actuators under equal-biaxial forces, uniaxial forces, and uniaxial constraint of stiff fibers *Soft Matter* **8** 6167–73

[18] Calabrese L, Frediani G, Gei M, De Rossi D and Carpi F 2018 Active compression bandage made of dielectric elastomers *IEEE-ASME Trans. Mechatronics* **23** 2328–37

[19] Hossain M, Vu D K and Steinmann P 2015 A comprehensive characterization of the electro-mechanically coupled properties of VHB 4910 polymer *Arch. Appl. Mech.* **vol 85** 523–37

[20] Cicconofri G and DeSimone A 2015 Motility of a model bristle-bot: a theoretical analysis *Int. J. Non-Linear Mech.* **7** 233–9

[21] Cicconofri G, Becker F, Noselli G, DeSimone A and Zimmermann K 2016 The inversion of motion of bristle bots: analytical and experimental analysis *CISM Lecture Notes No. 569—ROMANSY 21—Robot Design, Dynamics and Control* ed V Parenti-Castelli and W Schiehlen (New York: Springer) pp 225–32

[22] Clough R W and Penzien J 1993 *Dynamics of structures* (New York: McGraw-Hill)

[23] Perepechko I 1980 *Low-temperature properties of polymers* (Oxford: Pergamon)

[24] Illers K H and Jenckel E 1959 Dynamic mechanical behavior of polystyrene, poly-p-chlorostyrene, and poly-p-bromostyrene at low temperatures *J. Polym. Sci.* **41** 528–31

[25] Kiser J, Manning M, Adler D and Breuer K 2016 A reduced order model for dielectric elastomer actuators over a range of frequencies and prestrains *Appl. Phys. Lett.* **109** 133506

[26] Christensen R M 1971 *Theory of Viscoelasticity: An Introduction* (New York: Academic) pp 16–20

[27] Miles P, Hays M, Smith R and Oates W 2015 Bayesian uncertainty analysis of finite deformation viscoelasticity *Mech. Mater.* **91** 35–49